# Journal Pre-proof

Study of Early P91 Dual Corrosion in Steam and Simulated Combustion Gases from a Gas-Fired Boiler

Anibal Alviz-Meza, Adam Duong, Juan Orozco-Agamez, Viatcheslav Kafarov, Yulineth Cárdenas-Escorcia, Gaylord Carrillo-Caballero, Darío Peña-Ballesteros

Please cite this article as: Alviz-Meza A, Duong A, Orozco-Agamez J, Kafarov V, Cárdenas-Escorcia Y, Carrillo-Caballero G, Peña-Ballesteros D, Study of Early P91 Dual Corrosion in Steam and Simulated Combustion Gases from a Gas-Fired Boiler, *Journal of Materials Research and Technology*, https://doi.org/10.1016/j.jmrt.2021.04.071.

This is a PDF file of an article that has undergone enhancements after acceptance, such as the addition of a cover page and metadata, and formatting for readability, but it is not yet the definitive version of record. This version will undergo additional copyediting, typesetting and review before it is published in its final form, but we are providing this version to give early visibility of the article. Please note that, during the production process, errors may be discovered which could affect the content, and all legal disclaimers that apply to the journal pertain.

# Study of Early P91 Dual Corrosion in Steam and Simulated Combustion Gases from a Gas-Fired Boiler

Anibal Alviz-Meza[1]*, Adam Duong[2], Juan Orozco-Agamez[1], Viatcheslav Kafarov[3], Yulineth Cárdenas-Escorcia[4], Gaylord Carrillo-Caballero[5], Darío Peña-Ballesteros[1]

[1]*Grupo de Investigaciones en Corrosión, Escuela de Ingeniería Metalúrgica, Universidad Industrial de Santander, Bucaramanga, Colombia*
[2]*Institut de Recherche sur l'Hydrogène, Département de Chimie, Biochimie et Physique, Université du Québec, Trois-Rivières, Canada*
[3]*Grupo de Investigación CIDES, Escuela de Ingeniería Química, Universidad Industrial de Santander, Bucaramanga, Colombia*
[4]*Grupo de Investigación GIOPEN, Departamento de energía, Universidad de la Costa, Barranquilla, Colombia*
[5]*Grupo de Investigación en Energías Alternativas y Fluidos (EOLITO), Universidad Tecnológica de Bolivar, Cartagena, Colombia*

*E-mail address: anibalalvizm@hotmail.com

## Abstract

P91 ferritic steel pipes face dual environments during boilers operation: steam-side and fire-side. This P91 steel assessment differs from the dual studies performed to simulate coal-fired boilers -oxyfuel/steam atmospheres- since the fuel source is replaced by natural gas. This research work includes designing a device to reproduce dual corrosion studies at 650 °C and testing times up to 200 h. One coupon face was exposed to combustion gases while the other to steam. As a main result, the duplex's inner layer allowed to state that combustion gases overcome the steam oxidation rate by a factor of 1.6. Besides, we supplied physical-chemistry information about the surface and bulk of oxide layers by atomic force microscopy, scanning electron microscopy, x-ray photoelectron spectroscopy, and x-ray diffraction analysis. Thus, our experiments aimed to obtain data about the P91 early degradation under the simultaneous $72.73N_2/8.30CO_2/3.37O_2/15.60H_2O$ %mol and steam influence. We last for a future work the isolated evaluation of both environments to determine their role on the corrosion rate obtained in the current study.

## 1.   Introduction

The Fe-9Cr-1Mo alloy -also known as P91- belongs to the exclusive group of ferritic steels that have gained ground in the power generation industry due to its low coefficient of thermal expansion, efficient heat transfer, stress corrosion endurance, and thermal creep resistance up to 600 ºC [1-4]. However, some authors reported its premature failure outside design conditions [5], but also after being exposed to severe carburization-hydrogen attack [6], steam oxidation stresses, thermal conductivity drops, pipes blockages, and erosion problems [7,8].

In real operations, the power plant components are exposed to two different environments on opposite surfaces, water vapor (steam-side) and combustion gases (fired-side) in the case of boiler pipes. Corrosion research carried out under these conditions is called dual corrosion studies. These approximations allow obtaining estimates of the real deterioration of steels during their service, improving both the control and the safety of the process.

In this regard, Nakagawa *et al.* [9,10] found that between 550 and 650 ºC, the deterioration velocity of 9 %Cr ferritic steels is faster than in single oxidation atmospheres. They argued as well about hydrogen role and diffusion. Moreover, Chandra and Kranzmann [11] also Mosquera-Feijoo [12] presented a closer approach to the boiler's dual environment when replicated oxyfuel-steam atmospheres at 600 and 650 ºC, respectively. Chandra and Kranzmann also proposed in their work that

hydrogen diffusion from steam-side to the oxyfuel-side explains why dual kinetics is three times faster than in the single oxyfuel mixture of gases.

Although the dual corrosion of P91, or steels from the same family, has been addressed to simulate boilers working at 650 ℃, most research works have focused on boilers from coal-fired power plants. Therefore, the behavior of P91 steel in the dual environment of a gas-fired boiler -flue gas/steam- represents the novelty of our research study. Thus, we provide chemical results related to both corrosion sides and their early degradation rates.

## 2. Experimental

### 2.1 Experimental conditions

According to our previous study [13], we introduced the molar composition $72.73N_2/8.30CO_2/3.37O_2/15.60H_2O$ to simulate the fire-side stream within the furnace. Even though the boiler's mass flow was irreproducible, we implemented 2.15 g/h and 11.45 g/h for the steam and combustion gases mass flow, respectively. The water mass flow remained the same in both streams to compare the additional effect produced by the oxidizing species $CO_2$ and $O_2$ on the combustion side. The rest of the variables selected were 1 atm of pressure, simulating low pressure steam boiler at 650 ℃, and testing times of 1, 10, 20, 50, and 200 h.

### 2.2 Material

The P91 steel samples used for the experimental tests were obtained by cylindrical machining and wire cutting from a 15 cm long and 2.5 cm thick tube provided by *U.S. Metals*, whose composition was obtained by atomic emission spectroscopy (Table 1).

Table 1.  Chemical composition (wt-%) of P91 steel.

| Element | C | Mn | P | S | Si | Cr |
|---|---|---|---|---|---|---|
| % Weight | 0.106 | 0.316 | 0.013 | 0.003 | 0.768 | 8.439 |
| Element | V | N | Ni | Al | Nb | Mo |
| % Weigtht | 0.024 | 0.015 | 0.271 | 0.006 | 0.008 | 0.989 |

The final dimensions of the cylindrical coupons were 3 mm thick and 15 mm in diameter, with an exposed area of 1.33 $cm^2$ per face. The different samples evaluated were polished with silicon carbide paper until the mirror finish and subjected to an ultrasonic bath with acetone to avoid the impurities contributions.

## 2.3   Experimental setup

We used an argon stream to drag water from a bubbler at 73 °C towards the steam-side. The same procedure was applied to obtain the desire combustion gases, this time by humidifying the stream $86.2N_2/9.8CO_2/4.0O_2$ %mol. Electric heating cords assisted both flow lines, avoiding the condensation of steam before reaching the reactor. Lastly, the outer reactor, quartz tube, held the device in which the samples were inserted (see Fig.
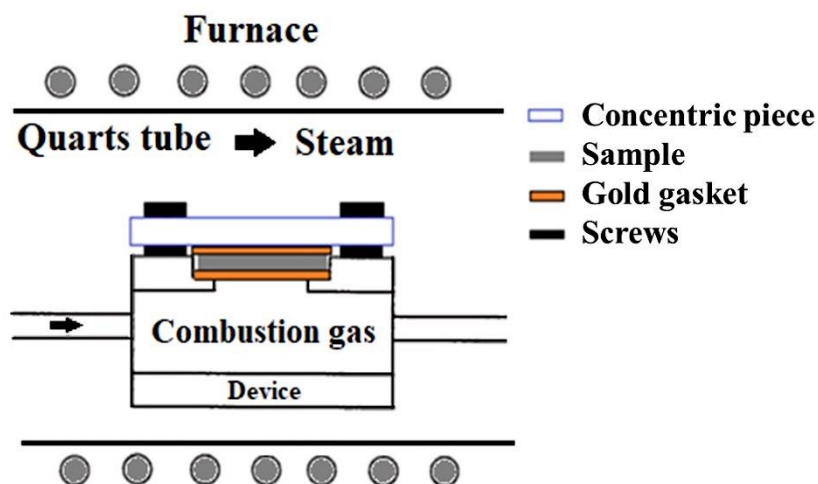
1).

Fig. 1 - Dual reactor setup.

We built the device using 316L stainless steel due to its well-known corrosion resistance. Then, gold seals were used to slow down the galvanic corrosion among P91 samples and the dual reactor's metallic parts. Furthermore, to guarantee the desired temperature inside the quartz tube, a thermocouple was introduced to perform its calibration before the experimental tests was carried out.

## 2.4 Characterization techniques

We rely on the following techniques to describe the surface and bulk corrosion products: scanning electron microscopy (SEM) with energy dispersive spectroscopy (EDS), X-ray diffraction (XRD), atomic force microscopy (AFM) and X-ray photoelectron spectroscopy (XPS). Table 2 presents explicit information about the different equipment and their operational parameters.

Table 2. Characterization equipment and its operational parameters.

| Technique | Equipment | Parameters |
|---|---|---|
| **SEM-EDS** | Quanta FEG 250, BSED-SSD, EDAX APOLO X | Voltage 25 kV, high vacuum, and detector resolution of 126.1 eV, Mn-K$\alpha$ |
| **XRD** | BRUKER D8 ADVANCE DaVinci geometry | Voltage 40 kV, current 40 mA, scan range between 10–70 °2θ, step size of 0.06 °2θ, and counting time of 1 s per step |
| **XPS** | SPECS: FOCUS 500, PHOIBOS150 2D-DLD | Monochromatic Al-K$\alpha$ x-ray source, the vacuum pressure of $10^{-9}$ atm, instrumental |

| | | broadening of 0.75 eV with adventitious carbon peak settled at 284.8 eV |
|---|---|---|
| **AFM** | Multimode Nanoscope III A | Scan size $10\mu m \times 10\mu m$ |

We introduced SEM-EDS to determine the morphology of the layers at the cross-section and surface. However, it also provided data related to their elemental composition and corrosion rates. AFM assisted the SEM images describing the topography at the top of the layer. XRD provided the crystalline phases at the scale bulk, and XPS the oxidation states onto de oxide layer and adsorption aspects. Further, we compare the corrosion rate found by SEM with the discontinuous gravimetric analysis.

## 3. Results and discussion

### 3.1 P91 Microstructure as received

As shown in Fig. 2, we received the P91 alloy with a ferritic microstructure after normalizing and tempering heat treatments. According to the Fe-Cr-C and isothermal transformation diagrams from Dunder *et al.* [14] and Durand-Charre [15], low cooling rates support the obtention of ferrite grains rich in carbides and carbo-nitrides. Carbides respond to the molecular formula $M_7C_3$ and $M_{23}C_6$ -M as Cr, Fe, Mn, Mo, Nb, and V- while carbo-nitrides to Nb, V(C, N) -this time M as Nb and V, while X as C and N- [16,17]. Additionally, the microstructure revealed high stability since the deposited grains were the smallest following the ASTM E112 grain size diagrams [18].
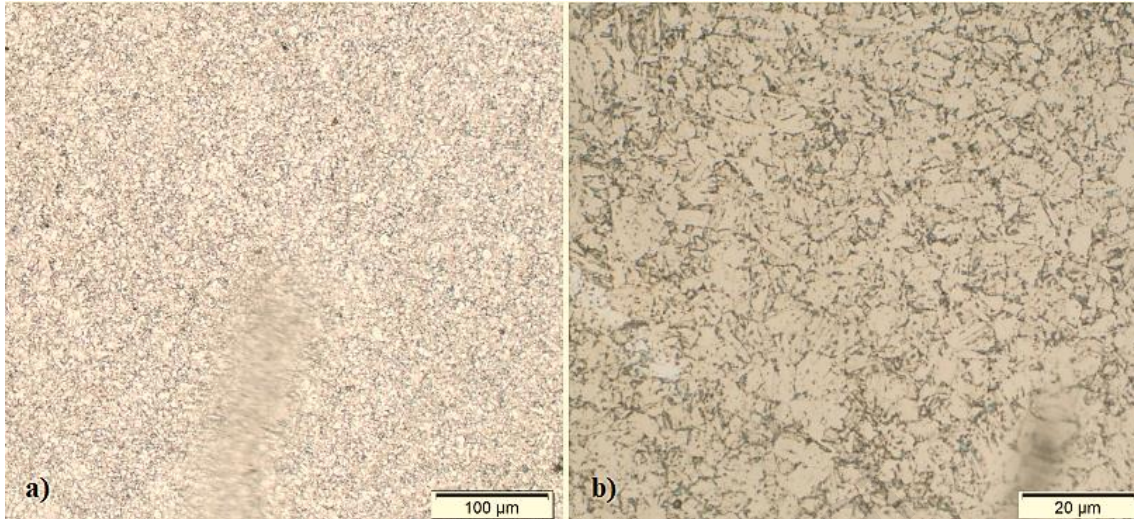
Fig. 2 - P91 microstructure as received.

## 3.2  P91 corrosion at room temperature (RT)

When oxidizing P91 steel at RT, even for short periods, a rapid nucleation of iron oxides (FeO · Fe$_2$O$_3$) and chromium oxides (Cr$_2$O$_3$) is generated, giving place to a nanometric layer of Fe-Cr spinel (Fig. 2 and Fig. 3). These binary mixed spinels are also described as Fe$^{+2}$(Fe$_{1-n}$Cr$_n$)$_2$O$_4$; where $0 < n < 1$ denotes the mole fraction of chromite: n = 1 is for pure chromite, and n = 0 for magnetite [19].

The Fe oxides Fe$^{+2}$ and Fe$^{+3}$ were evidenced at one-broad energetic peak located at Fe 2p$_{3/2}$ ~708,8 eV -magnetite- according to Moulder's XPS handbook [20] and the NITS database [21]. This scale was of few nanometers since the pure metal peak at Fe 2p$_{3/2}$ ~706 eV overcame its intensity (see Fig. 3). The Fe$^0$ energetic region was fitted by three couple of peaks -multiplets- attending to the well-accepted Fe 2p deconvolution [22].
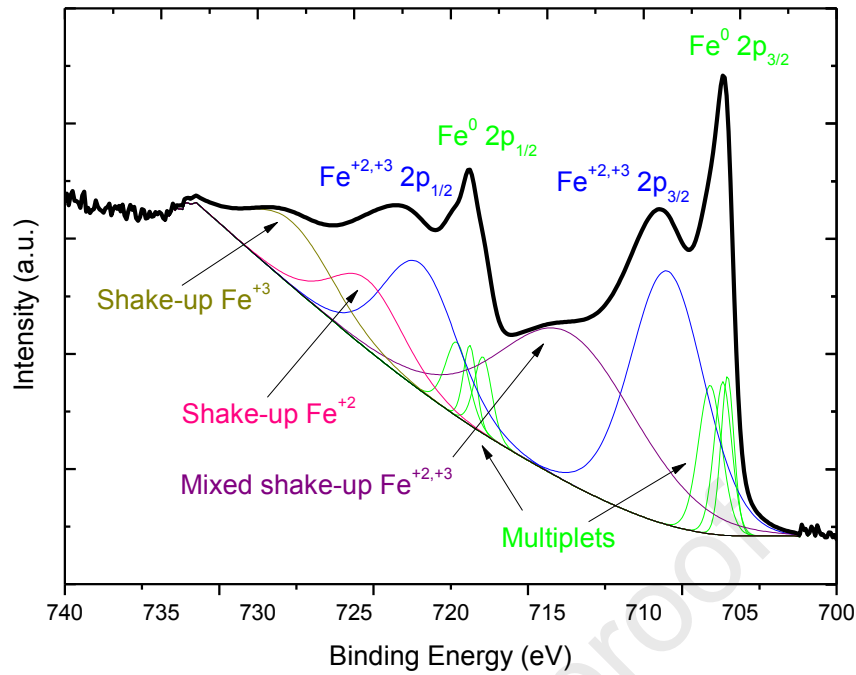
Fig. 3 - Fe 2p region from P91 oxidation at room temperature.

Fig. 4 shows the oxidation states $Cr^0$ and $Cr^{+3}$ at Cr $2p_{3/2} \sim 573.3$ eV and Cr $2p_{3/2} \sim$ 576.1 eV, respectively. The graphic suggests that the oxide intensity was more representative than the metal one, pointing out a strong presence of $Cr_2O_3$ within the oxide layer. Therefore, we settle that the Fe-Cr spinel scale is the equilibrium structure at RT. However, it was also clear that 9% of Cr is insufficient to avoid Fe diffusion. Other findings regarding the absence of metal elements such as Mn and Mo were associated with their lower weight amount in the received alloy.
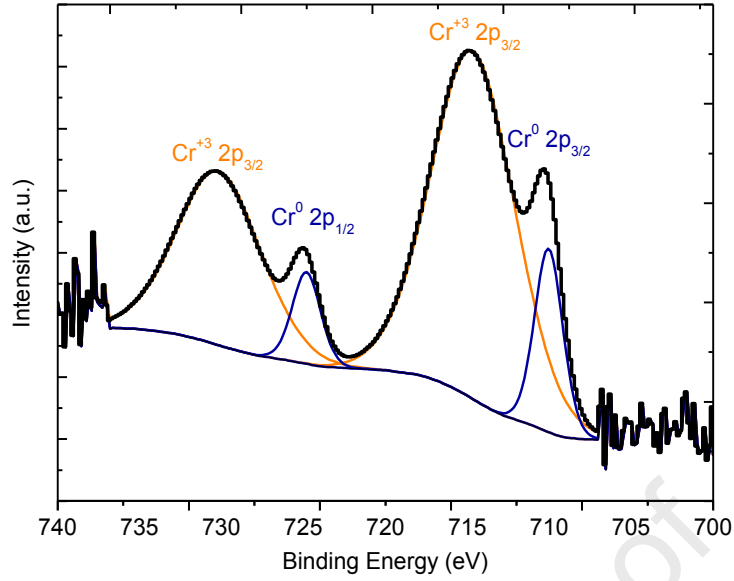
Fig. 4 - Cr 2p region from P91 oxidation at room temperature.

The discussion about the corrosion mechanism induced by both steam and combustion gases is argued independently in the section, offering a comprehensive analysis of each corrosive environment by comparing our results with the actual background of P91 corrosion at high temperatures. Although, we compiled the kinetic data and the corrosion rates behind the same-titled section.

### 3.3  Diffusion and corrosion rate

The layers' growth responded to a parabolic kinetic law. This trend implies that oxide scales grew by a diffusive mechanism (see Fig. 5), where metal cations contribute actively to the alloy corrosion rate initially but slow-down their contribution over time since the transport routes become hard to goes through. Then, we used Wagner's expression [23] to describe this behavior in Eq.(1):

$$X^2 = 2k_p t \tag{1}$$

Where $X$ denotes the mass gain per unit area or the thickness of the layer, $t$ the time, and $k_p$ the parabolic constant.
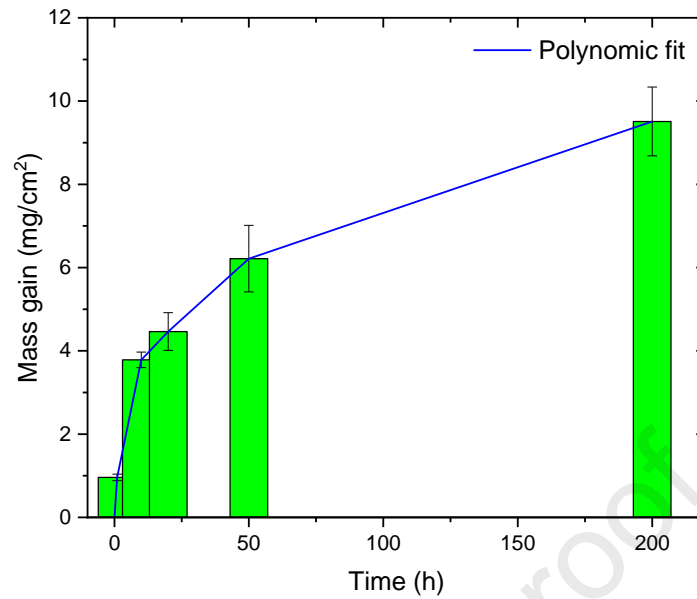
Fig. 5 - Parabolic growth law followed by P91 samples under the dual environment.

The corrosion rate for each corrosion side was calculated (Fig. 6) based on the measurements of their inner layer's thickness and by following the NACE RP 0775 standard [24], which fixes the onset of severe corrosion at 0.25 mm/year. The corrosion rate was higher on the combustion side by a factor of 1.6 due to the superior oxygen potential conferred by $CO_2$ and $O_2$. However, both deterioration velocities were found severe. In the long term, once the stationary state is reached, we expect smaller values and a more accurate P91 assessment.
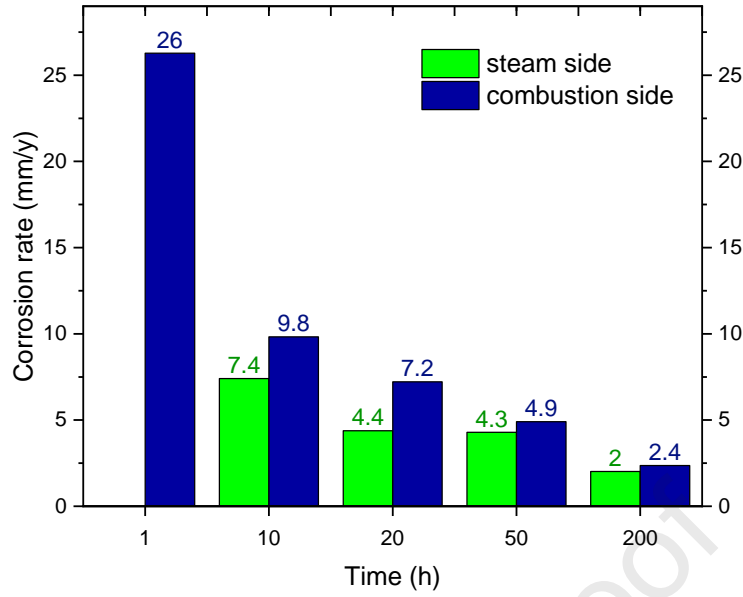
Fig. 6 - Corrosion rate at combustion and steam sides.

Further, we determined a mathematical expression to relay the parabolic kinetic constant from both oxide layers in Eq.(3) by rearranging Eq.(1) and Eq.(2). For instance, the kinetic constants obtained for each layer on the combustion side were: $K_i = 14.6 \ \mu m^2 h^{-1}$ and $K_e = 21.2 \ \mu m^2 h^{-1}$, confirming the higher corrosion rate of the external layer, as we discuss later in Fig. 15.

$$X_T = X_e + X_i \qquad (2)$$

$$K_T = K_e + 2\sqrt{K_e K_i} + K_i \qquad (3)$$

### 3.4  P91 corrosion on the steam side

Nucleation of Cr and Fe oxides on the steam-side uncover the complete P91 sample's surface after short exposure times (Fig. 7). Instead, we observed remarkable participation of secondary elements such as Mo and Mn. But even more outstanding for Mn, which demonstrated lower activation energy than Mo at 650 ℃, despite its limited weight amount in the alloy.
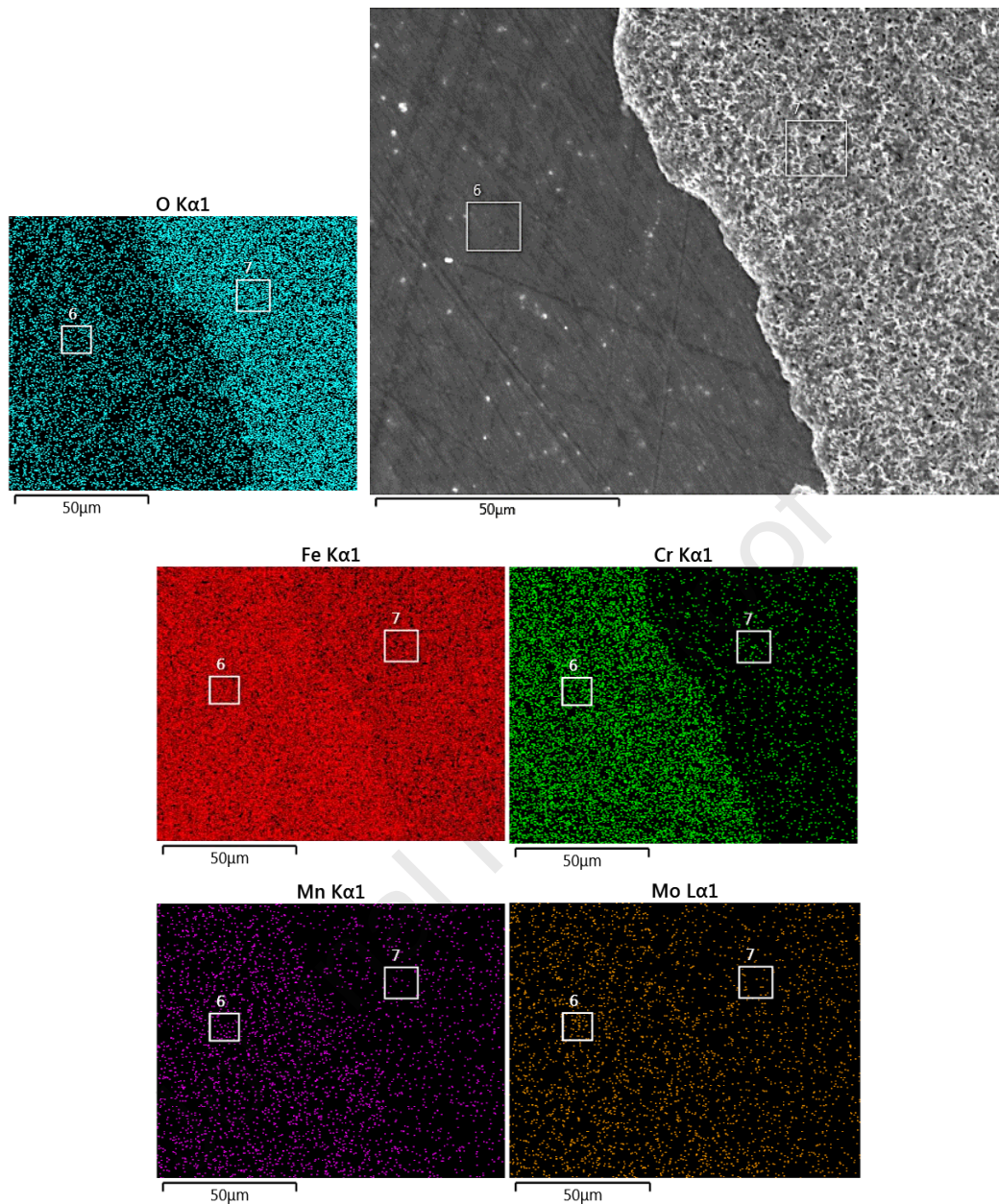
Fig. 7 - Surface SEM micrograph in the back-scattered electron mode after 1 h at the steam side.

The Fe and Mn staging is often related to the limited Cr response capacity caused by its insufficient weight in the alloy [25]. This phenomenon is similar to the *breakaway oxidation* [26], which is nothing more than the condensation of fissures through the chromium oxide layer to favor fast Fe diffusion and its poorly protective oxide layers. This mechanism would be promoted by a direct reaction of steam molecules with the

metal surface because Cr oxidizes internally rather than in the form of a protective external scale (Fig. 8) [27].
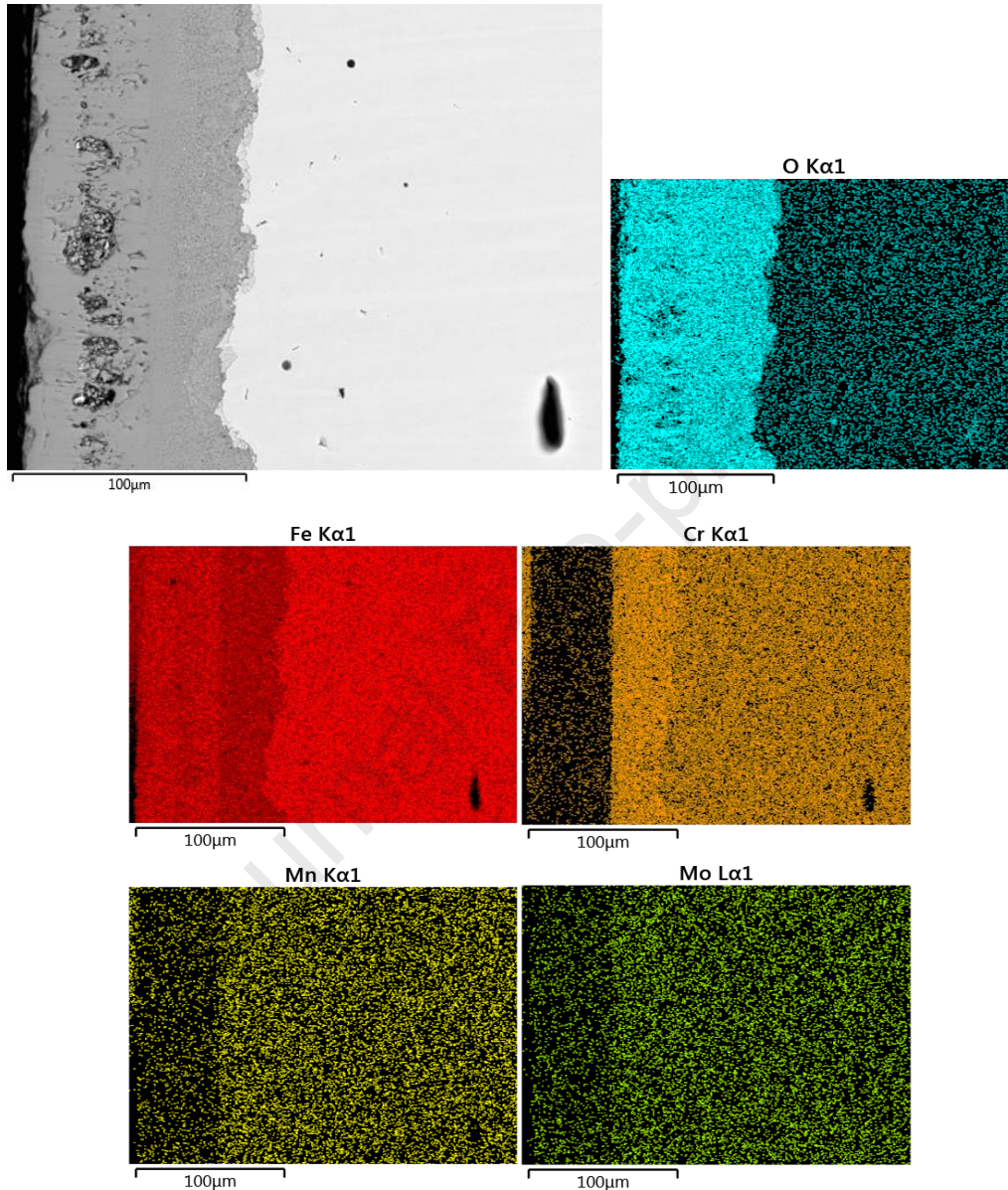


Fig. 8 - Cross-section SEM micrograph in the back-scattered electron mode after 200 h at the steam side.

As suggested by Quadakkers *et al.* [28], Fig. 8 shows a duplex structure of oxides at 650 °C after 200 h. We support that idea since the smooth line that separates the two layers is observable, as much as their different morphologies, Cr amounts, and brightness

intensities. The inner layer is made of Fe, Cr, Mn, Mo, and O, possibly forming mixed spinels, while the outer layer mainly of iron oxides. Traces of Mn and Mo among the layers respond to their localized oxides, presented as evidence of the strong influence of diffusive processes.

P91 steam oxidation has promoted multiple research works, which have aimed to identify the role of some adverse effects over the duplex oxide layer [29,30]. Water vapor tends to accelerate the depletion of Cr at the metal matrix interface and along with the layers due to the volatilization of iron and chromium oxides [31-34], which together with the high cation diffusion contribute to the release of multiple vacant sites, leading to the appearance of pores and gaps. In turn, those "empty spaces" respond to their mass transport mechanism, $H_2O/H_2$ bridges [26,35], causing pores coalescence [36], big-gaps, microcracks, and macrocracks; increasing the inward and outward molecular transfer.

We found a slight domain of cations diffusion over the transport of oxidant species along with the layers. The outer layer grew faster than the inner, as shown in Fig. 9. It is partially explained either by the well-adherence and less fissured inner layer, opposite to the weak outer layer in Fig. 10. In this regard, authors such as Martinelli *et al.* [36] have proposed that $H_2O/OH^*$ take advantage of the "available space" left by cations, and accumulated by hydrogen trapping, to stimulate the growth of internal oxides. Moreover, Oleksak *et al.* [37] proved the existence of such microchannels through the technique of *Atom Probe Tomography* at the internal oxidation zone (Fig. 11) while Ehlers *et al.* [26] confirmed the dissociation of $H_2O$ mostly at the outer layer, but also reaching the matrix interface.
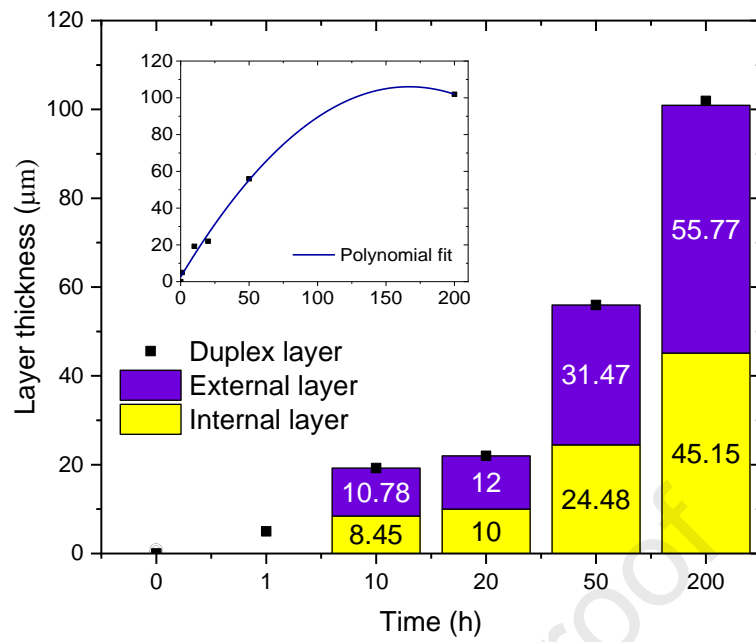
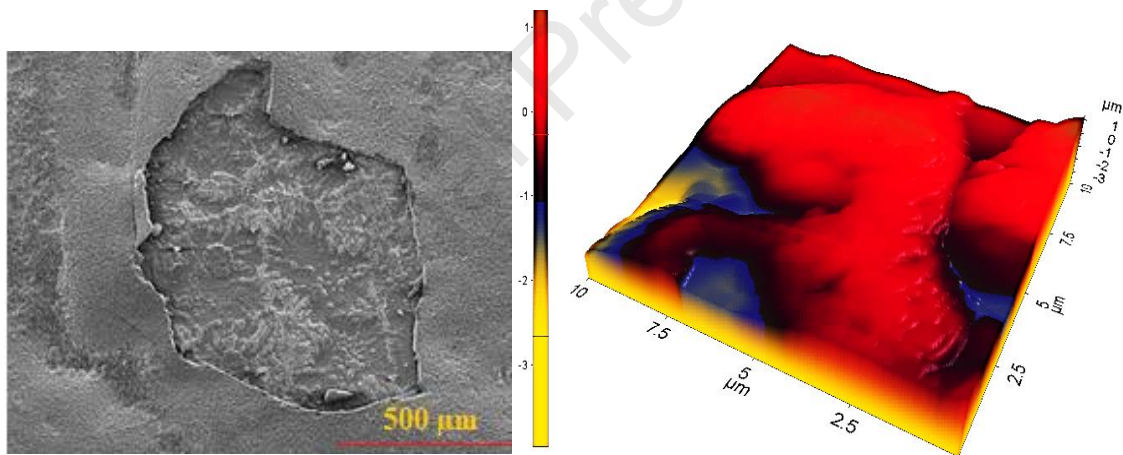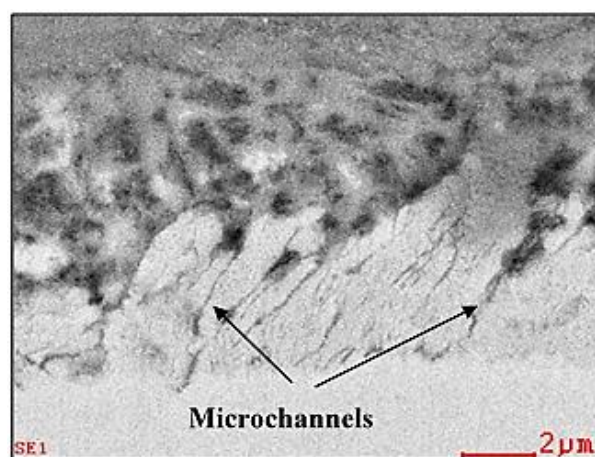Fig. 9 - Thickness growing overtime at the steam side.



Fig. 10 - SEM-AFM images of the oxide layers' surface after 200 h at the steam side.

Fig. 11 - SEM micrograph of the internal oxidation zone at the steam side after 20 h.

The diffusion of metal cations also produces Mo, Mn, and V oxides at the top of the

scales associated with $Mo^{+6}$, $Mn^{+2}$, $Mn^{+4}$, and $V^{+4}$, which correspond to $MoO_3$ at ~232 eV, $VO_2$ at ~516 eV, and $MnO$-$MnO_2$ at ~641 eV (Fig. 12).
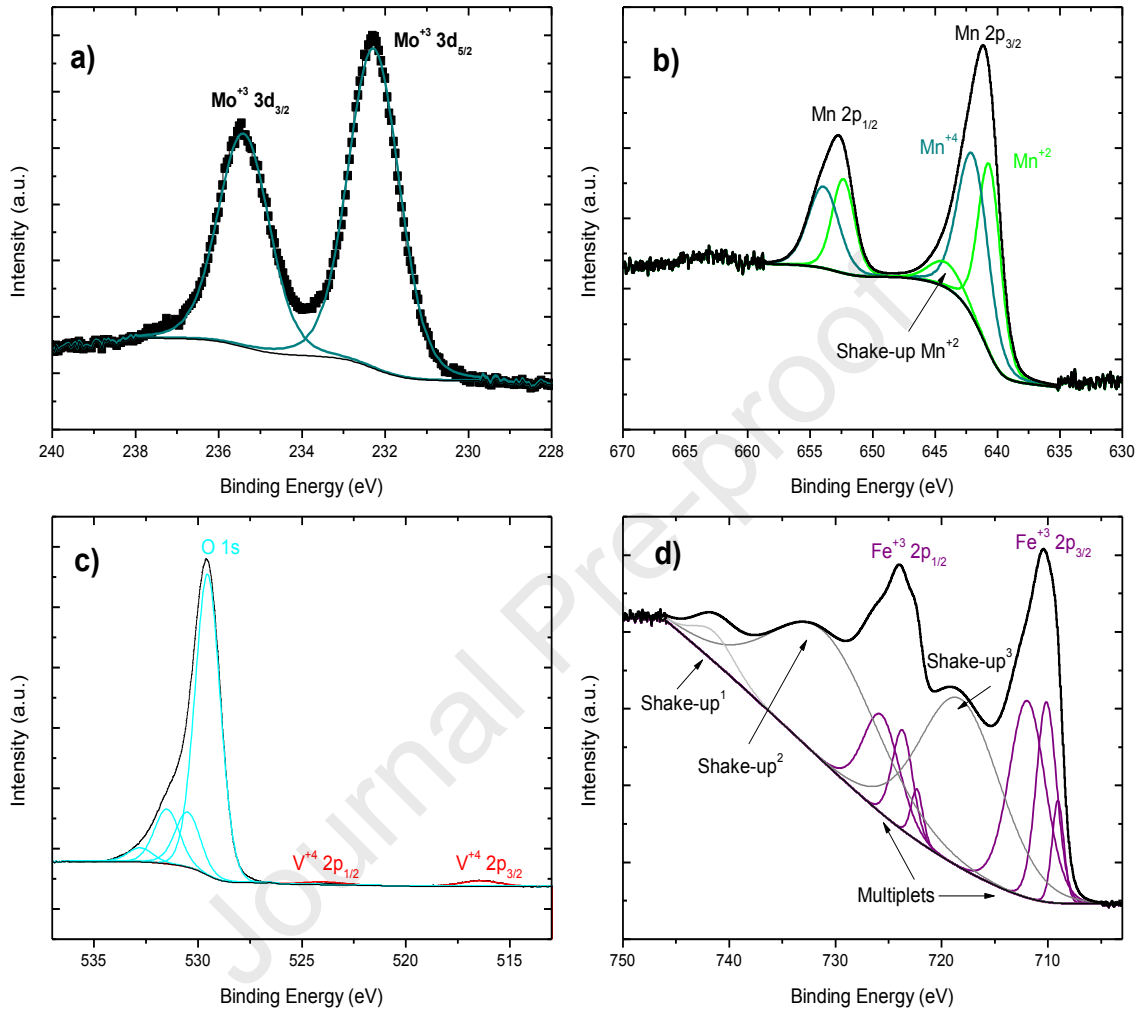


Fig. 12 - Regions identified by XPS after 200 h at the steam side: a) Mo 3d, b) Mn 2p, c) V 2p and d) Fe 2p.

Also, we confirmed that hematite is the iron oxide in thermodynamic equilibrium with the oxidizing environment since it was superficially located while magnetite and chromite were deposited on the layers' bulk (Fig. 8, Fig. 12 (d), and Fig. 13). Therefore, the proposed structure of layers is the following: hematite on the outer layer, magnetite on the intermediate layer, and chromite, Mn, Mo, and even V oxides on the internal one

(Fig. 12). Comparable results have been obtained before, but neither of them reporting superficial Mo and V oxides [29,36,38-40]. They also declaring $Cr_2O_3$ and FeO oxides at the internal oxidation zone [27]. These results differ from the spinel scale grown at RT, Fig. 3 and Fig. 4, since magnetite and chromite were displaced to the inner layer, which allows us to state that the P91 oxide scale is temperature dependent.
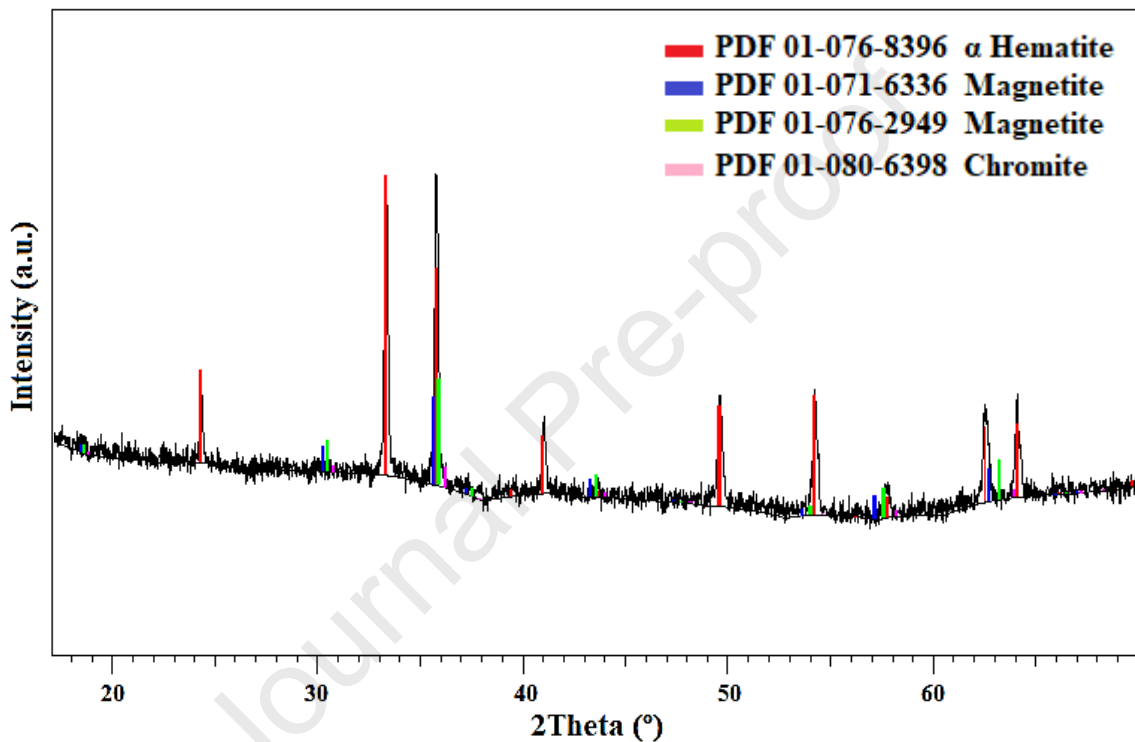


Fig. 13 - XRD spectra for specimen oxidized in steam for 200 h at 650 °C.

## 3.5 P91 corrosion on combustion side

Adding $CO_2$, $O_2$, and $N_2$ to steam disturbs the explained oxidation mechanism by introducing nitrides and carbides [41]. $CO_2$ and $N_2$ react with oxygen to produce $NO_x$ and $CO_x$ at high temperatures. These molecules use microchannels and lattice diffusion through the layers to feed internal corrosion processes. The microchannels are more

likely to be used across the outer layer but helped by the ions' lattice diffusion through the inner layer (Fig. 8).

Equal to steam side results, after 1 h of exposure to the combustion side, we also found an incomplete nucleation process, but this time covering a higher area. The initial layer structure resulted from the Cr retention followed by a posterior Fe diffusion. Although, Mn and Mo cations also took advantage of the chromium retention to be quickly oxidized but in less quantity, proportional to their mass amount in the steel. Thus, the early spinel layer obtained was a cocktail of mixed oxides (Fig. 14).
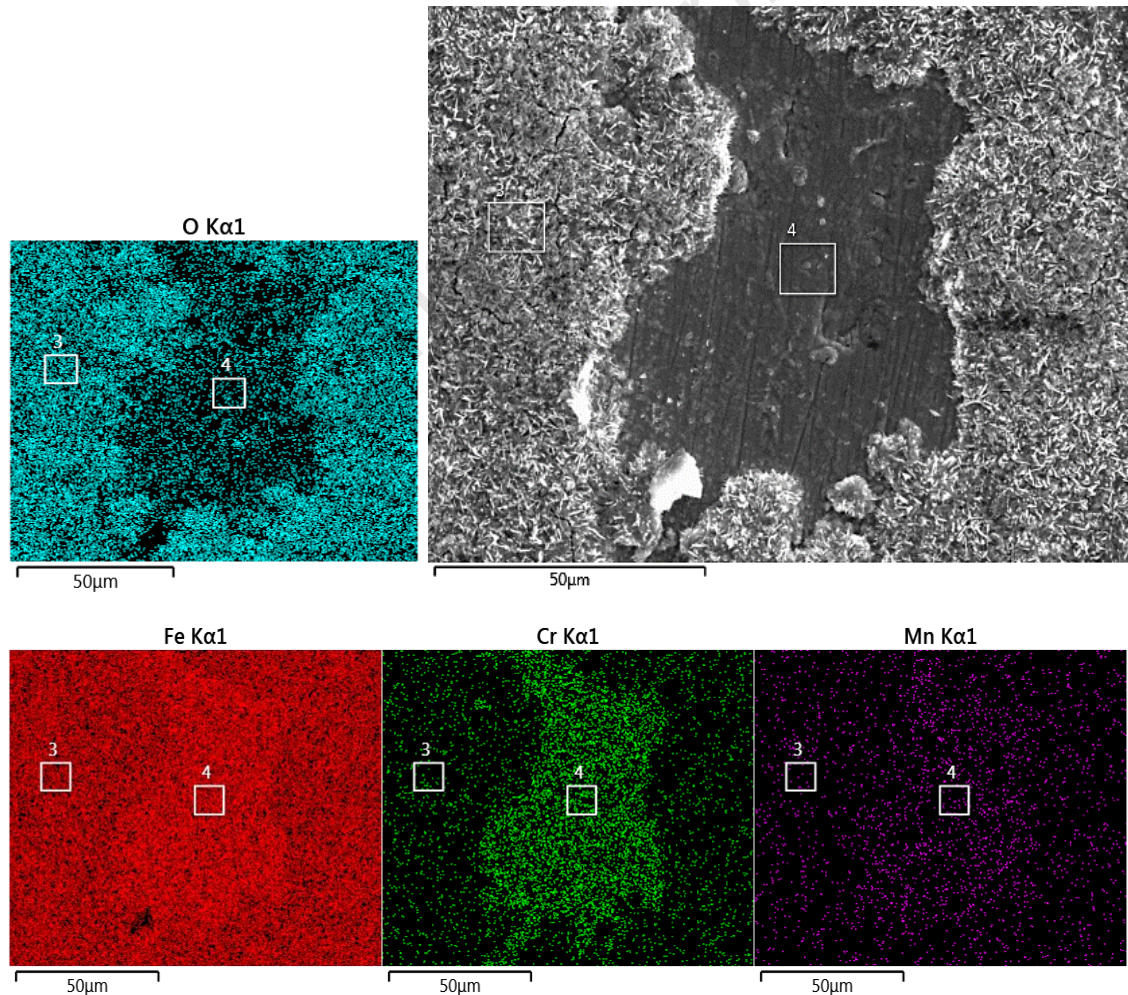


Fig. 14 - Surface SEM micrograph in the back-scattered electron mode after 1 h at the combustion side.

The outer layer was found thicker than the obtained on the steam side after 200 h (Fig. 15). It is a direct consequence of the additional presence of $O_2$ and $CO_2$ regarding the single steam environment. These molecules increased the oxygen potential, favored the transport of species across layers, and postponing the formation of internal carbides up to 1000 h of exposure [25,42].
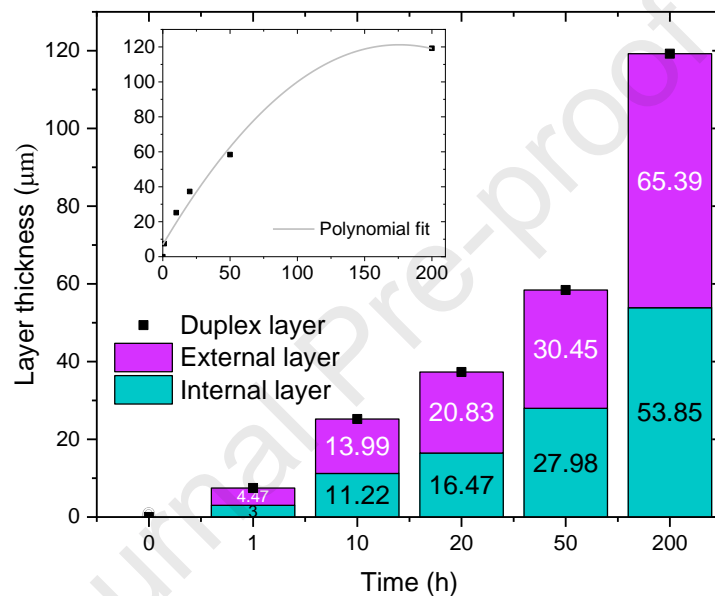


Fig. 15 - Thickness growing overtime at the combustion side.

$NO_x$ and $CO_x$ require morphology fissures to reach the base metal and favorable dissociation conditions. The first request seems to be well-covered by the high porosity and gaps condensed throughout the external layer (Fig. 16), while $NO_x$ and $CO_x$ achieve the second at the scale/oxide interface, as reported by Martinelli *et al.* [36]. The authors also established this carburization mechanism, where analogous to $H_2$, carbon gets trapped at the metal interface until carbide precipitation. The same idea applies to nitrides, becoming mass transport in a vastly competitive process. Moreover, Taylor *et*

*al.* [43] proved the entry of $CO_2$ to the alloy matrix by experimentally monitoring $C^{16}O_2$ and $C^{18}O_2$ isotopes, thus favoring the *Boudouard reaction* to stimulate the internal carburization [44]. Concerning nitridation phenomena, nitrogen atoms are steemed to be transported by nitrates through microchannels (Fig. 15) until the metal interface, where the low oxidation potential and the accumulation of nitrogen would promote the internal precipitation of nitrides [13,45].
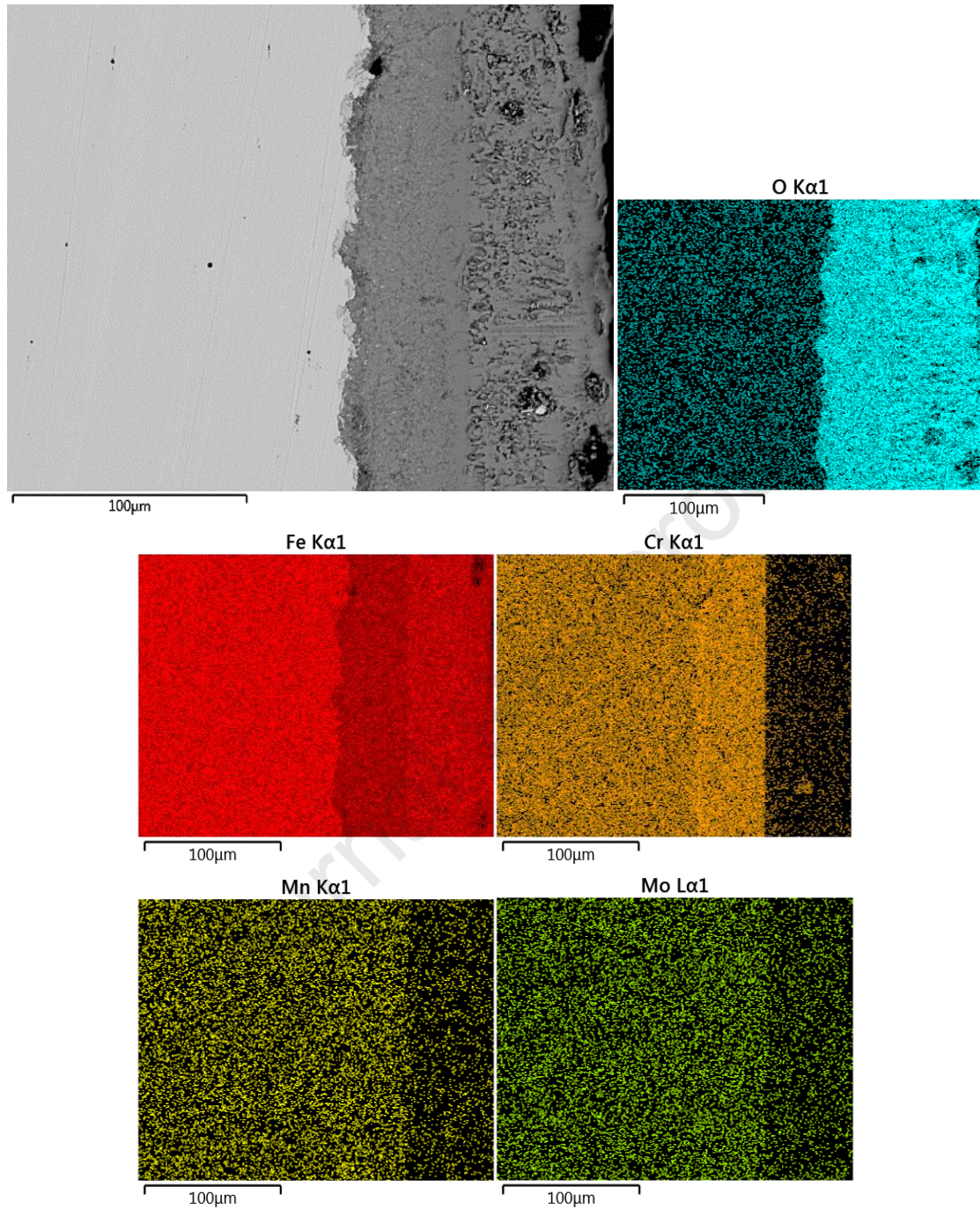
Fig. 16 - Cross-section SEM micrograph in the back-scattered electron mode after 200 h at the combustion side.
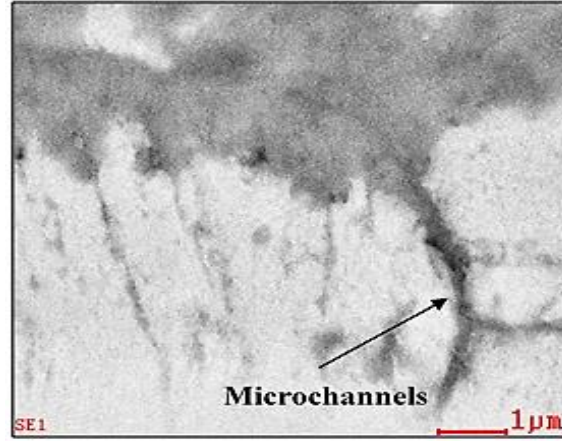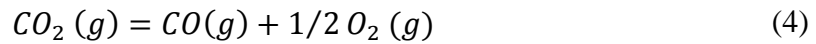
Fig. 17 - SEM micrograph of the internal oxidation zone after 20 h at the combustion side.

Likewise, we decided to neglect diffusion as the driven mechanism. For this purpose, the reaction of Boudouard (Eq.5) was used to describe the release of carbon from the gaseous environment [44]. The Eqs.(7-8) were introduced as the thermodynamic support of Eqs.(4)-(5) [23] with $P_{O_2} = 3.37 \cdot 10^{-2} atm$ and $P_{CO_2} = 8.30 \cdot 10^{-2} atm$ at 650 °C. As a result, the studied environment was decarburizing to the alloy ($a_{c,gas} < a_{c,P91}$) [46], since $a_{c,gas} = 1.10 \cdot 10^{-22}$ while $a_{c,P91}$ for $\alpha$-phase has been reported to be $1.50 \cdot 10^{-3}$ according to Kaya $et$ $al.$ [47] close to 650 °C. However, we made our numerical estimate based on the P91 surface carbide $Cr_7C_3$ [17,47], assuming $a_{Cr_7C_3} = 1$ and $a_{Cr} = 0.089$ -%mol of Cr in the alloy- [46]. This time obtaining $a_{c,P91} = 1.76 \cdot 10^{-9}$ through Eq.(6) and Eq.(9) at 650 °C [23,44].

$$CO_2\ (g) = CO(g) + 1/2\ O_2\ (g) \tag{4}$$

$$2CO\ (g) = CO_2(g) + C \tag{5}$$

$$7/3\ Cr + C = 1/3\ Cr_7C_3 \tag{6}$$

$$\Delta G° = -RTln\left(P_{CO}P_{O_2}^{0,5}\middle/P_{CO_2}\right), with\ \Delta G° = 282420 - 86{,}8T\ (J/mol) \tag{7}$$

$$\Delta G^{\circ} = -RTln\left(\frac{P_{CO_2}a_{c,gas}}{P^2_{CO}}\right), with\ \Delta G^{\circ} = -170700 + 174,5T\ (J/mol) \tag{8}$$

$$\Delta G^{\circ} = -RTln\left(\frac{a^{\frac{1}{3}}_{Cr_7C_3}}{a^{\frac{7}{3}}_{Cr}a_{c,P91}}\right), with\ \Delta G^{\circ} = -174509 - 25.5T\ (J/mol) \tag{9}$$

On the other hand, we found surface carbides at ~283 eV and nitrides at ~387 eV (Fig. 18). These compounds are superficially rarely reported under oxidizing environments [34,38,42,44,48] whereby we suggest that chemical and physical adsorption phenomena led to such compounds.
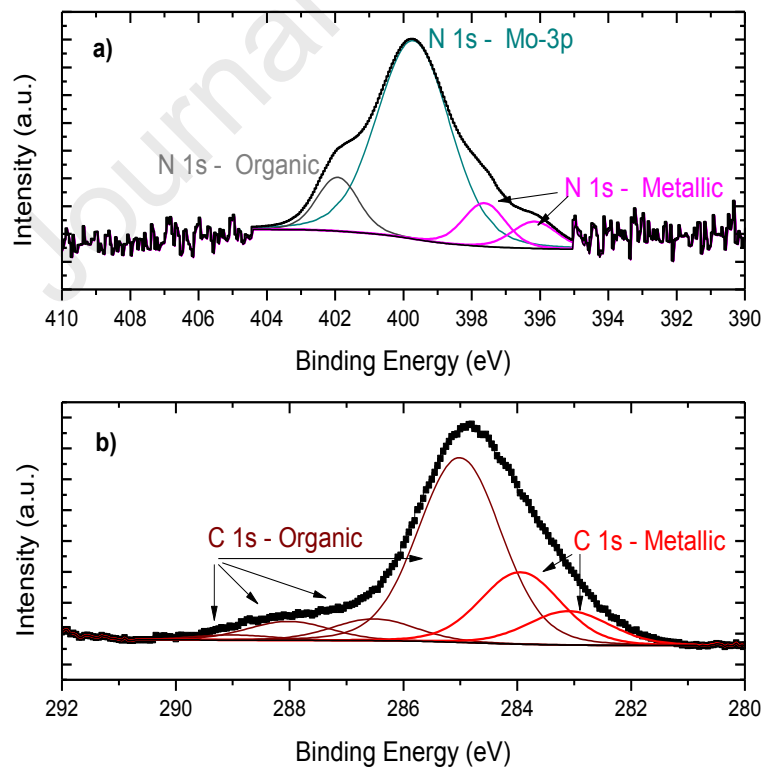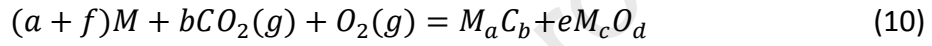


Fig. 18 – (a). N 1s and (b). C 1s regions identified by XPS at the combustion side after 200 h at 650 ºC.

Namely, NO and $CO_2$ are the molecules linked to adsorption processes due to their polarity and availability, though $H_2O$ is adsorbed preferably according to its larger dipole moment: $H_2O > CO_x > NO_x$ [54]. Eqs.(10-11) show the global expressions involved, where $M$ denotes the metal cations, letters from $a$ to $d$ atomic coefficients, $e = 2(b + 1)/d$, $f = e \cdot c$, $g = (b + 2)/d$, and $h = g \cdot c$. Oxides such as those presented in Fig. 12 would be formed at 650 ℃, favored by standard Gibbs energies but relegated nitrides and carbides to discrete sites. Either way, they could be discomposed, oxidized, and volatilized.

$$(a + f)M + bCO_2(g) + O_2(g) = M_aC_b + eM_cO_d \qquad (10)$$
$$(a + h)M + bNO(g) + O_2(g) = M_aN_b + gM_cO_d \qquad (11)$$

## 4. Conclusions and future work

In this research work, we focused on describing the early corrosion process of P91 steel into the simulated dual combustion-gas/steam environment from an industrial boiler. The experimental conditions settled were 650 ℃, 1 atm of pressure, and exposure times up to 200 h. The oxide structure deposited on the alloy was found time and temperature-dependent. Meanwhile, the outward diffusion of cations controlled the oxidation rate of the steel in both environments. At room temperature, the single oxide scale was made of spinel. But at 650 ℃, the duplex structure gave place to surface hematite with bulk magnetite on the outer layer, while chromite, Mn, and Mo oxides on the inner one. Both corrosive environments gave place to the surface oxides: $MnO_2$, $MnO$, $MoO_3$, and $VO_2$. Although the fire-side scale also introduced surface nitrides and carbides to the scale due to the adsorption of $CO_2$ and $NO_x$ molecules. It allowed stating that mass-transfer processes are such relevant as adsorption phenomena to understand the corrosion of alloys at high temperatures. Additionally, the P91 corrosion rate was 1.6 faster at the fire-side than at the steam-side in coherence with the additional contribution of $CO_2$ and

O$_2$ gases. Finally, long-term trials, internal corrosion processes, adsorption phenomena, and the influence of one environment on the other are issues left for future works.

**Acknowledgements**

## 5.  References

[1]    T. Sasaki, K. Kobayashi, T. Yamaura, T. Kasuya, and T. Masuda, "Production and properties of seamless modified 9Cr-1Mo steel boiler tubes," *Kawasaki Steel Tech. Rep.*, vol. 25, pp. 78–87, 1991.

[2]    I. Le May, "Creep and fracture of engineering materials and structures," *Mater. Charact.*, vol. 33, p. 79, 2003.

[3]    F. Noble, B. Senior, and B. Eyre, "The effect of phosphorus on the ductility of 9Cr-1Mo steels," *Acta Metall. Mater.*, vol. 38, no. 5, pp. 709–717, May 1990.

[4]    H. Nickel, P. J. Ennis, and W. J. Quadakkers, "The creep rupture properties of 9% chromium steels and the influence of oxidation on strength," *Miner. Process. Extr. Metall. Rev.*, vol. 22, no. 1–2, pp. 181–195, 2001.

[5]    A. Fabricius and P. Jackson, "Premature Grade 91 failures — worldwide plant operational experiences," *Eng. Fail. Anal.*, pp. 1–9, 2016.

[6]    G. Ju, W. Wu, and S. Dai, "Failure of 9Cr-1Mo tubes in a feed furnace of dehydrogenation unit," *Int. J. Press. Vessel. Pip.*, vol. 74, no. 3, pp. 199–204, 1997.

[7]    T. Kurniawan, F. A. B. Fauzi, and Y. P. Asmara, "High-temperature oxidation of fe-cr steels in steam condition − A review," *Indones. J. Sci. Technol.*, vol. 1, no. 1, pp. 107–114, 2016.

[8]    A. Shibli and F. Starr, "Some aspects of plant and research experience in the use of new high strength martensitic steel P91," *Int. J. Press. Vessel. Pip.*, vol. 84, no. 1–2, pp. 114–122, 2007.

[9]    K. Nakagawa, Y. Matsunaga, and T. Yanagisawa, "Corrosion behavior of ferritic steels on the air sides of boiler tubes in a steam/air dual environment," *Mater. High Temp.*, vol. 20, no. 1, pp. 67–73, 2003.

[10]   K. Nakagawa, Y. Matsunaga, and T. Yanagisawa, "Corrosion behavior of ferritic steels on the air sides of boiler tubes in a steam/air dual environment," *Mater. High Temp.*, vol. 18, no. 1, pp. 51–56, 2001.

[11]   K. Chandra and A. Kranzmann, "High temperature oxidation of 9 – 12 % Cr ferritic /martensitic steels under dual-environment conditions," *Corros. Eng. Sci.*

*Technol.*, vol. 53, no. S1, pp. 27–33, 2018.

[12] M. Mosquera-Feijoo, "Influence of surface ash layer on dual corrosion," Doctoral dissertation, Universidade de Vigo, Vigo, 2019.

[13] A. Alviz-Meza, V. Kafarov, and D. Y. Peña-ballesteros, "Evaluation of Corrosion Damage Obtained During the Combustion Process in a Boiler. Case Study : Ferritic ASTM A335 P91 Steel," *Chem. Eng. Trans.*, vol. 70, pp. 1093–1098, 2018.

[14] M. Dunder, I. Samardzic, and T. Vuherer, "Weldability investigation steel P91 by weld thermal cycle simulation," *Metalurgija*, vol. 54, no. 3, pp. 539–542, 2015.

[15] M. Durand-Charre, "The basic phase diagrams," in *The Microestructure of Steels and Cast Irons*, Ed. Springer, pp. 51–73.

[16] N. E. Zavaleta, H. De Cicco, and C. Danón, "Influencia del tiempo de revenido a 780 °C sobre la resistencia al creep del acero ASTM A335 P91," *Materia*, vol. 23, no. 2, pp. 1–8, 2018.

[17] T. Gheno *et al.*, "Carburisation of ferritic Fe-Cr alloys by low carbon activity gases," *Corros. Sci.*, vol. 53, no. 9, pp. 2767–2777, 2011.

[18] ASTM Internacional, "Standard Test Methods for Determining Average Grain Size: E112 - 10," 2004.

[19] K. Delura, P. Bylina, M. Jele, and J. Kruczyk, "Mineralogy and magnetism of Fe – Cr spinel series minerals from podiform chromitites and dunites from Tapadła ( Sudetic ophiolite , SW Poland) and their relationship to palaeomagnetic results of the dunites," *Geophys. J. Int.*, vol. 175, pp. 885–900, 2008.

[20] J. Moulder, W. Stickle, P. Sobol, and K. Bomben, *Handbook of X-Ray Photoelectron Spectroscopy*. Eden Prairie, United States of America: Perkin-Elmer Corporation, 1992.

[21] NITS, "National Institute of Standards and Technology NIST X-ray Photoelectron Spectroscopy (XPS) Database," 2012. [Online]. Available: https://srdata.nist.gov/xps/main_search_menu.aspx. [Accessed: 30-Mar-2021].

[22] M. Bravo, J. Huerta, D. Cabrera, and A. Herrera, "Composition assessment of ferric oxide by accurate peak fitting of the Fe 2p photoemission spectrum," *Surf. Interface Anal.*, vol. 49, no. 4, pp. 253–260, 2016.

[23] D. Young, *High temperature oxidation and corrosion of metals*, 1st ed. Cambridge: Department of Materials Science and Metallurgy, University Cambridge, 2008.

[24] NACE International, "Standard Recommended Practice: Preparation, Installation, Analysis, and Interpretation of Corrosion Coupons in Oilfield Operation," Houston, RP 0775, 2005.

[25] G. Meier *et al.*, "Effect of Alloy Composition and Exposure Conditions on the Selective Oxidation Behavior of Ferritic Fe-Cr and Fe-Cr -X Alloys," *Oxid. Met.*, vol. 74, no. 5–6, pp. 319–340, 2010.

[26] J. Ehlers *et al.*, "Enhanced oxidation of the 9%Cr steel P91 in water vapour containing environments," *Corros. Sci.*, vol. 48, no. 11, pp. 3428–3454, 2006.

[27] J. Quadakkers, W.J., Zurek, "Shreir's Corrosion: Oxidation in Steam and Steam / Hydrogen Environments," vol. 1, pp. 407–456, 2010.

[28] W. J. Quadakkers, P. J. Ennis, J. Zurek, and M. Michalik, "Steam oxidation of ferritic steels - Laboratory test kinetic data," *Mater. High Temp.*, vol. 22, no. 1–2, pp. 47–60, 2005.

[29] S. Saunders, M. Monteiro, and F. Rizzo, "The oxidation behaviour of metals and alloys at high temperatures in atmospheres containing water vapour: A review," *Prog. Mater. Sci.*, vol. 53, no. 5, pp. 775–837, 2008.

[30]    P. Ennis and W. Quadakkers, *Mechanisms of oxidation and the influence of steam oxidation on service life of steam power plant components*, Cambridge: Woodhead Publishing, 2008.

[31]    F. Pérez and S. Castañeda, "Study of oxyhydroxides formation on P91 ferritic steel and CVD-FBR coated by Al in contact with Ar + 40% $H_2O$ at 650 °C by by TG-mass spectrometry," *Surf. Coat. Technol.*, vol. 201, pp. 6239–6246, 2007.

[32]    F. Pérez and S. Castañeda, "Study by means of the mass spectrometry of volatile species in the oxidation of Cr, $Cr_2O_3$, Al, $Al_2O_3$, Si, $SiO_2$, Fe and ferritic/martensitic steel samples at 923 K in Ar+(10 to 80%)$H_2O$ vapor atmosphere for new-materials design," *Oxid. Met.*, vol. 66, no. 5–6, pp. 231–251, 2006.

[33]    E. J. Opila, N. S. Jacobson, D. L. Myers, and E. H. Copland, "Predicting oxide stability in High-Temperature Water Vapor," *Jom*, vol. 58, no. January, pp. 22–28, 2006.

[34]    M. Michalik, M. Hansel, J. Zurek, L. Singheiser, and W. J. Quadakkers, *Effect of water vapour on growth and adherence of chromia scales formed on Cr in high and low*, vol. 67. Forschungszentrums Jülich, 2007.

[35]    A. Rahmel and J. Tobolski, "Einfluss von wasserdampf und kohlendioxyd auf die oxydation von eisen in sauerstoff bei hohen temperaturen," *Corros. Sci.*, vol. 5, no. 5, pp. 333–346, 1965.

[36]    L. Martinelli, C. Desgranges, F. Rouillard, K. Ginestar, M. Tabarant, and K. Rousseau, "Comparative oxidation behaviour of Fe-9Cr steel in $CO_2$ and $H_2O$ at 550 °C : detailed analysis of the inner oxide layer," *Corros. Sci.*, vol. 100, pp. 253–266, 2015.

[37]    R. P. Oleksak, M. Kapoor, D. Perea, G. Holcomb, and O. Dogan, "The role of metal vacancies during high-temperature oxidation of alloys," *npj Mater. Degrad.*, vol. 2, no. 1, p. 25, 2018.

[38]    S. Swaminathan, C. Mallika, N. Gopala, C. Thinaharan, T. Jayakumar, and K. Mudali, "Evolution of surface chemistry and morphology of oxide scale formed during initial stage oxidation of modified $9Cr - 1Mo$ steel," *Corros. Sci.*, vol. 79, pp. 59–68, 2014.

[39]    C. Anghel, E. Hörnlund, G. Hultquist, and M. Limbäck, "Gas phase analysis of CO interactions with solid surfaces at high temperatures," *Appl. Surf. Sci.*, vol. 233, no. 1–4, pp. 392–401, 2004.

[40]    K. Chandra, I. Dörfel, N. Wollschläger, and A. Kranzmann, "Microstructural investigation using advanced TEM techniques of inner oxide layers formed on T92 steel in oxyfuel environment," *Corros. Sci.*, vol. 148, pp. 94–109, 2019.

[41]    X. Zheng and D. Young, "High-Temperature Corrosion of $Cr_2O_3$-Forming Alloys in $CO$-$CO_2$-$N_2$ Atmospheres," *Oxid. Met.*, vol. 42, pp. 163-190, 1994.

[42]    J. Piro, T. Olszewski, H. Penkalla, G. Meier, L. Singheiser, and W. Quadakkers, "Scale formation mechanisms of martensitic steels in high $CO_2$/$H_2O$-containing gases simulating oxyfuel environments," *Mater. High Temp.*, vol. 26, no. 1, pp. 63–72, 2009.

[43]    M. R. Taylor, J. M. Calvert, D. G. Lees, and D. B. Meadowcroft, "The Mechanism of Corrosion of Fe-9 % Cr Alloys in Carbon Dioxide," *Oxid. Met.*, vol. 14, no. 6, pp. 499–516, 1980.

[44]    T. Gheno, D. Monceau, J. Zhang, and D. J. Young, "Carburisation of ferritic Fe-Cr alloys by low carbon activity gases," *Corros. Sci.*, vol. 53, pp. 2767–2777, 2011.

[45]    A. Alviz-Meza, J. Sanabria-Cala, V. Kafarov, and D. Y. Peña-Ballesteros, "Study

of Continuous Corrosion on ASTM A335 P91 Steel in an Environment of $CO_2$-$O_2$-$N_2$-$H_2O$ Derived from the Theoretical Combustion Products of a Mixture of Refining Gases at High Temperatures," *Chem. Eng. Trans.*, vol. 70, pp. 1069–1074, 2018.

[46] G. Lai, *High Temperature Corrosion And Materials Applications*, 1st ed. ASM Internacional, 2007.

[47] K. Kaya, S. Hayashi, and S. Ukai, "High-temperature Oxidation Behavior of 9Cr Ferritic-steel in Carbon Dioxide," *ISIJ Int.*, vol. 54, no. 6, pp. 1379–1385, 2014.

[48] X. G. Zheng and D. J. Young, "Corrosion of pure in $CO$-$CO_2$-$SO_2$-$N_2$ atmospheres," *Corros. Sci.*, vol. 36, no. 12, pp. 1999–2015, 1994.

**Declaration of interests**

☒ The authors declare that they have no known competing financial interests or personal relationships that could have appeared to influence the work reported in this paper.

☒The authors declare the following financial interests/personal relationships which may be considered as potential competing interests: